Electronic Supplementary Information

Local Magnetic Spin Mismatch Promoting Photocatalytic Overall Water Splitting with Exceptional Solar-to-Hydrogen Efficiency

Yiyang Li [a], Zihan Wang [b], Yiqi Wang [b], András Kovács [c], Christopher Foo [a], Rafal E. Dunin-Borkowski [c], Yunhao Lu [d], Robert A. Taylor [e], Chen Wu * [b] and Shik Chi Edman Tsang * [a]

[a] Wolfson Catalysis Centre, Department of Chemistry, University of Oxford, Oxford, OX1 3QR, UK

[b] School of Materials Science and Engineering, State Key Laboratory of Silicon Materials, Zhejiang University, Hangzhou, 310027, China

[c] Ernst Ruska-Centre for Microscopy and Spectroscopy with Electrons and Peter Grünberg Institute, Forschungszentrum Jülich, 52425 Jülich, Germany

[d] Zhejiang Province Key Laboratory of Quantum Technology and Device, Department of Physics, Zhejiang University, Hangzhou, 310027, China

[e] Clarendon Laboratory, Department of Physics, University of Oxford, Oxford, OX1 3PU, UK

*Correspondence to: edman.tsang@chem.ox.ac.uk; chen_wu@zju.edu.cn

Content

Supplementary Methods

Supplementary Methods

Materials

The reagents used in this work are the following: Titanium dioxide (Degussa P25, 75% anatase, 25% rutile); Titanium(IV) Tetra-Iso-Propoxide (TTIP, reagent grade, Sigma-Aldrich); Iron(III) nitrate nonahydrate (reagent grade, Sigma-Aldrich); Iron(II) chloride (reagent grade, Sigma-Aldrich); Hydrogen tetrachloroaurate trihydrate (reagent grade, Sigma-Aldrich); Isopropanol (99.9%, Sigma-Aldrich); Methanol (anhydrous, ≥ 99.8% (HPLC), Sigma-Aldrich); Acetic acid (reagent grade, Sigma-Aldrich); H_2SO_4 (≥ 98%, Sigma-Aldrich); Ammonia gas (anhydrous, BOC); Argon gas (99.99%, BOC); Helium gas (99.99%, BOC); Nitrogen gas (99.99%, BOC).

X-ray diffraction (XRD)

XRD measurements were performed on a Bruker D8 Advance diffractometer with LynxEye detector and Cu Kα1 radiation (λ= 1.5406 Å), operating at 40 kV and 25 mA (step size at 0.019°, time per step at 0.10 s, total number of steps at 4368). Samples were pressed onto a glass preparative slide and scanned at 2^{θ} angles of 5-90°.

X-ray photoelectron spectroscopy (XPS)

XPS measurements were carried out on the Thermo Scientific model Nexsa. The aluminium anode tube for the X-ray emission was operated at a voltage of 12 kV and kept constant during all measurements. Survey scans were obtained at a pass energy of 200 eV, 5 scans with step size 1 eV, whereas for those detailed spectra 50 eV pass energy, 10 scans with 0.1 eV step size were used. The XPS depth profiling was performed by etching the sample with Ar sputtering. The sample was etched with 3 keV Ar^+ ions at an angle of incidence (ϑ) of 45° to the normal surface of the sample. Etching time was varied to obtain the information of different depths, as shown in Fig. 1f in the main text.

Electron paramagnetic resonance (EPR)

Continuous-wave EPR spectra were obtained by using an X-band (9.4 GHz) Bruker EMX EPR spectrometer. All measurements were carried out at 293 K. 10 mg powder of each sample was weighed and put into a glass EPR tube (0.60 i.d. and 0.84 o.d.). Then all X-Band spectra were collected over a 7000 Gauss field range and 5 scans were adopted for each measurement. Signal intensity vs. electron spin numbers were calculated from the double integral of a defined peak range of the spectra.

Ultraviolet-visible diffuse reflectance spectroscopy (UV-vis DRS)

UV-vis DRS spectra were obtained from a Perkin Elmer Lambda 750S UV-visible spectrometer at room temperature. 50±5 mg of each sample was loaded and pressed onto a sample holder and UV-vis spectra were recorded within the wavelength range of 250-1100 nm.

Time-resolved photoluminescence (TRPL) spectroscopy

Photoluminescence spectra and corresponding lifetimes of excitons were obtained from a bespoke micro-photoluminescence setup, in which a Ti-Sapphire laser (λ = 266 nm, pulse duration = 150 fs, repetition rate = 76 MHz) was directed onto the sample. Time-resolved measurements were performed using the spectrometer as a monochromator before passing the selected signal to a photomultiplier tube (PMT) detector with an instrument response function width of ~150 ps connected to a time-correlated single-photon counting module.

The exciton lifetime is obtained by fitting corresponding background-corrected PL spectra with a mono-exponential decay function of the form $y = A_1 \exp(-x/t_1) + y_0$. Errors in the fitting were determined using a least square method.

Magnetisation curve measurements (M-H curve)

MPMS static magnetic properties of the samples were measured using a superconducting quantum interference device (SQUID, Quantum Design -XL-5).

Correlative off-axis electron holography and EDX mapping

The samples were studied using an electron probe aberration corrected transmission electron microscope (ThermoFisher Titan 80-200 ChemiSTEM) operated at 200 kV and equipped with in-column energy dispersive X-ray (EDX) spectroscopy and high-angle annular dark-field (HAADF, Fischione) detectors. The samples were hosted in a double-tilt sample holder dedicated for EDX measurements. The EDX spectral images were recorded with a typical dwell time of 10 μs and a spectral region of approximately 500 × 500 px using a cross-correlated drift correction. The acquisition and processing were carried out using the Velox software (ThermoFisher) following a calculation based on Cliff-Lorimer factors.

Off-axis electron holography experiments were carried out using an image aberration corrected transmission electron microscope (ThermoFisher Titan 60-300) operated in magnetic field free conditions at 300 kV. Electron holograms were recorded using a single biprism and a direct electron counting detector (Gatan K2 IS) at 4k resolution. The fringe spacing and contrast were approximately 2.5 nm and 30 %, respectively. The turning over experiments for electron holography were carried out using a modified tomography holder (Fischione).[1] The conventional Fourier transformation-based processing was used to process the electron holograms in order to get the corresponding electrical and magnetic phase shift images of the particles. The processing was carried out using a custom-made software package written in SEMPER language.
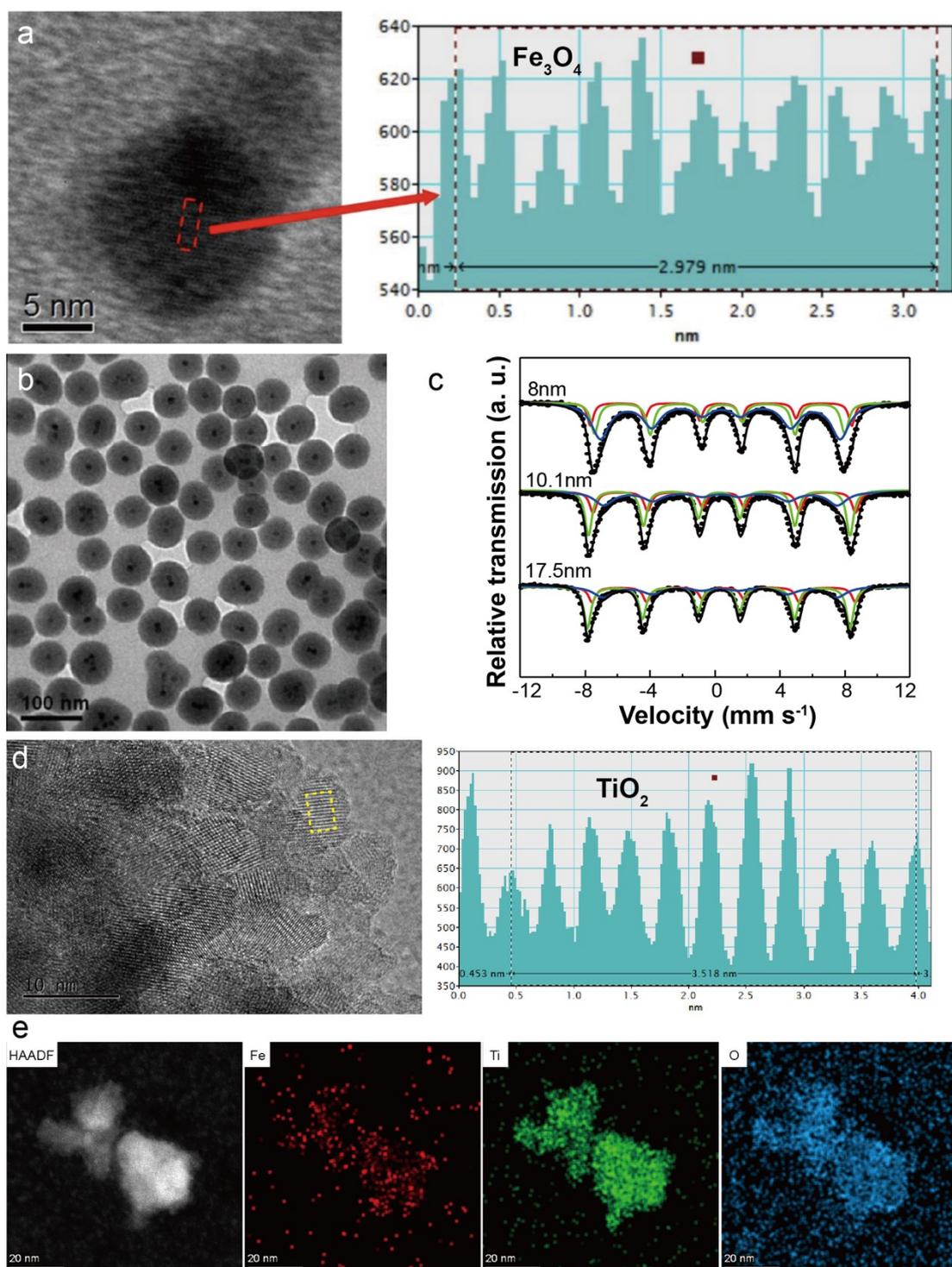
Figure S1 Microscopic characterisations **a** HR-TEM image of an Fe_3O_4 NP, for which the lattice spacing is 0.298 nm, corresponding to the (220) plane of Fe_3O_4 structure;[2] **b** TEM image of $Fe_3O_4@SiO_2$; **c** Mössbauer spectra of the Fe_3O_4 NPs with different mean particle sizes (black: collected overall response curves; blue and red (superparamagnetic): Fe_3O_4 phase; green: Fe_2O_3 phase); **d** HR-TEM images of $Fe_3O_4/N-TiO_2-2$ showing the lattice spacing of 0.352 nm which can be attributed to the anatase TiO_2 (101); **e** HAADF-STEM image of $Fe_3O_4/N-TiO_2-2$ and the corresponding energy dispersive X-ray spectroscopy (EDS) mapping. See Supplementary Discussion 2 for the details.
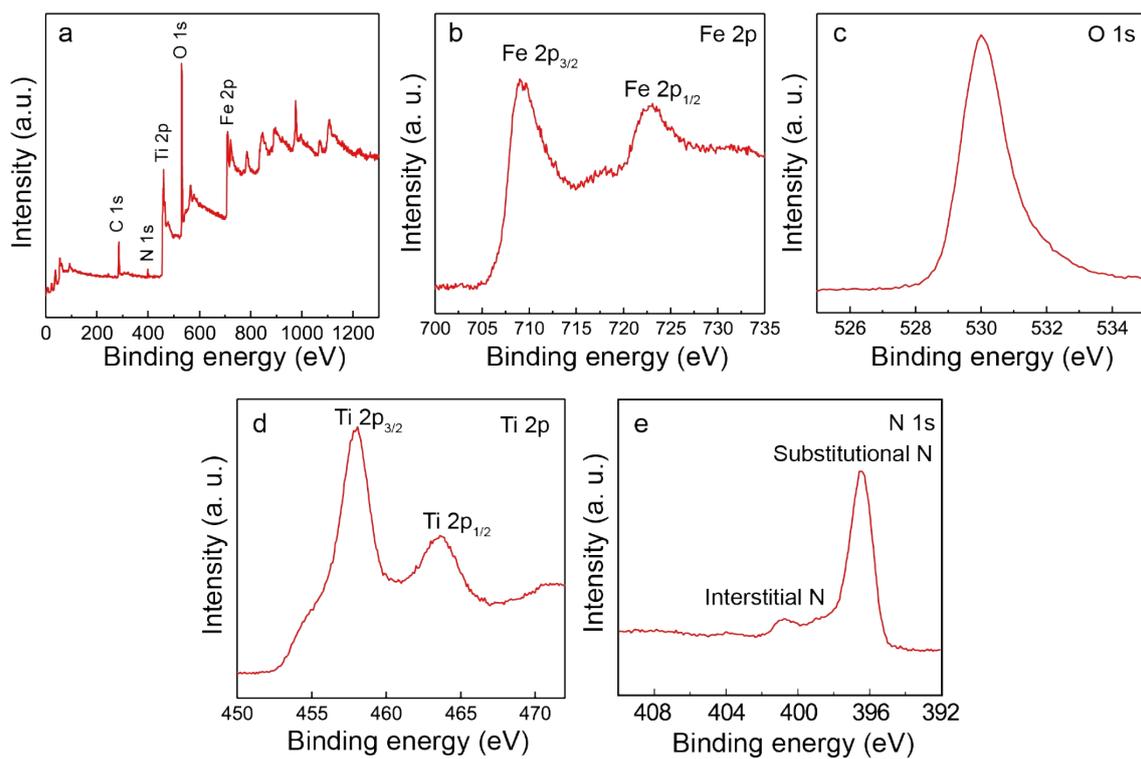
Figure S2 XPS spectra of Fe_3O_4/N-TiO_2-2. **a** Survey spectrum; **b** Fe 2p spectra; **c** O 1s spectra; **d** Ti 2p spectra and **e** N 1s spectra.
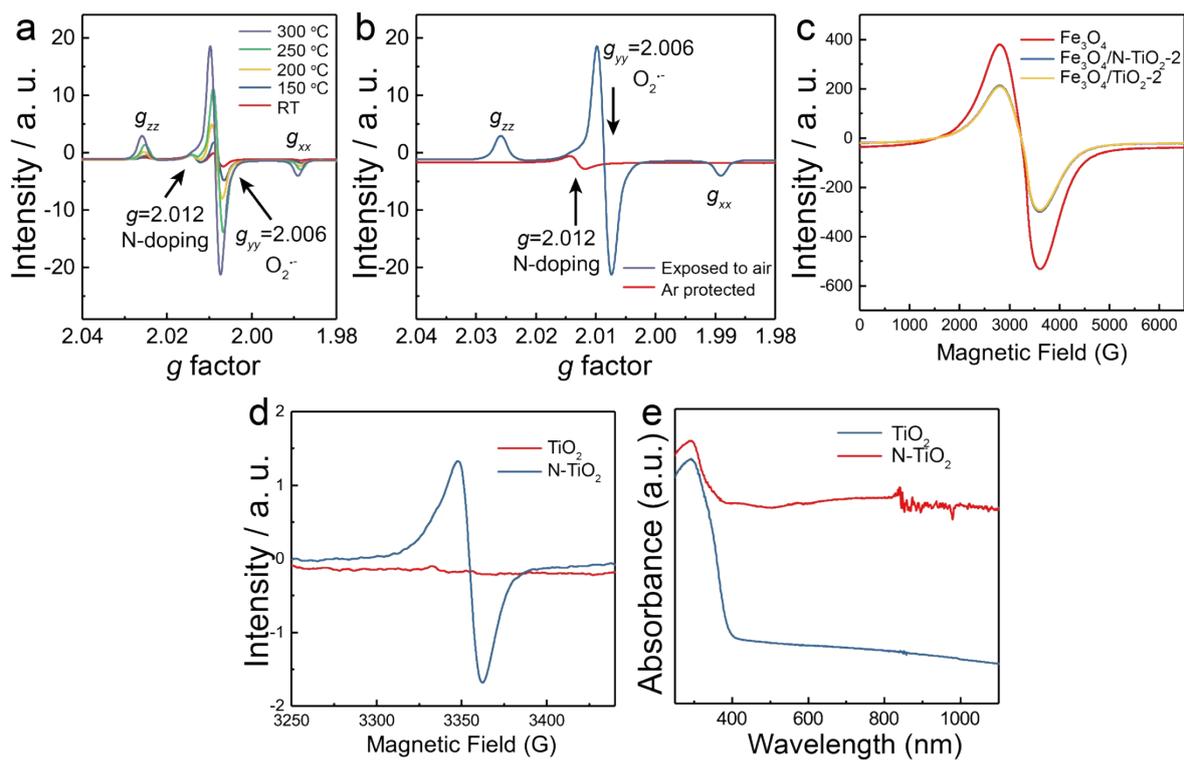
Figure S3 Spectroscopic study of the N-TiO$_2$ based photocatalysts. **a, b** Continuous-wave EPR spectra were obtained by using an X-band (9.39 GHz) Bruker EMX EPR spectrometer. All measurements were carried out at 293 K quenched from the high-temperature treatment in Ar, collected over a 7000 Gauss field range and 5 scans were adopted for each measurement. **c** selected field-scanning cw-EPR spectra of Fe$_3$O$_4$ NPs, Fe$_3$O$_4$/N-TiO$_2$-2 and Fe$_3$O$_4$/TiO$_2$-2; **d** selected field-scanning cw-EPR spectra of N-TiO$_2$ and TiO$_2$. **e** UV-vis diffuse reflectance spectra within the wavelength range of 250-1100 nm at room temperature.
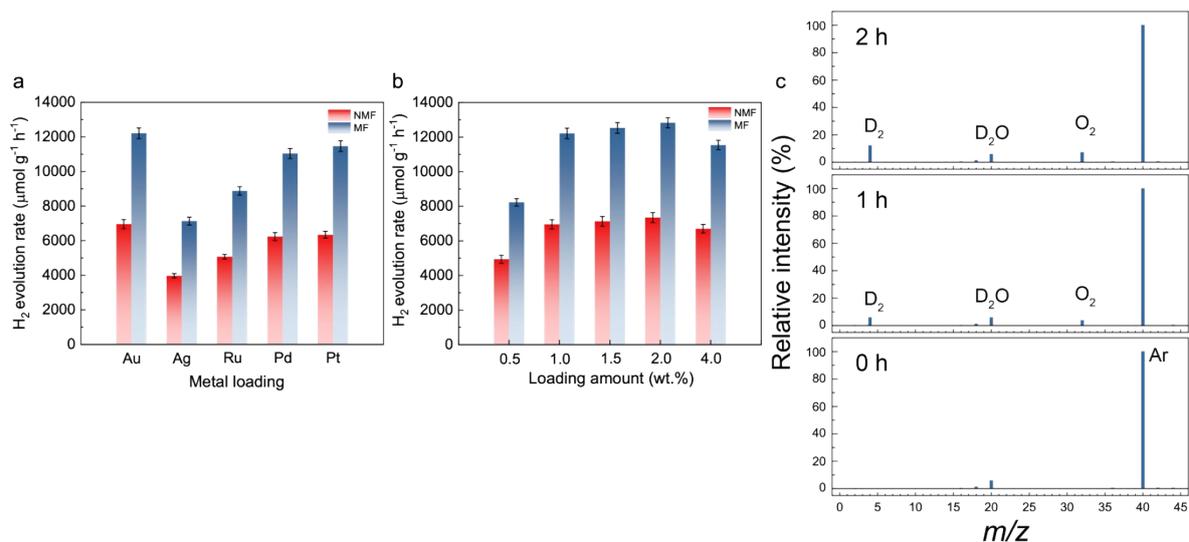
Figure S4 Study of metal loadings on the Fe_3O_4/N-TiO_2-2 photocatalyst. **a** POWS performance of the Fe_3O_4/N-TiO_2-2 photocatalyst decorated with 1 wt.% of different metal NPs via a photo-deposition method. **b** POWS performance of the Au-decorated Fe_3O_4/N-TiO_2-2 photocatalyst with different loading amounts. **c** Isotopic study of the POWS reaction on Fe_3O_4/N-TiO_2-2 photocatalyst decorated with 1 wt.% of Au NPs. The products were measured by mass spectrometer (Hiden Analytical) after certain reaction time, as indicated in the figure. All signals are re-scaled by the signal of the inert component Ar (The relative intensity of Ar is 100 %). As shown, before the reaction, the majority of the gaseous phase is the inert Ar gas (m/z=40), while the signal at m/z=20 and 18 can be assigned to the D_2O vapour. After the reaction of 1 hour, the signals of D_2 (m/z=4) and O_2 (m/z=32) are observed, while the signal of H_2 (m/z=2) is absent. Also, no N_2 signal was detected, which again, indicates that there is no mixed air in the system. When the reaction was performed for another 1 hour, the signals of D_2 and O_2 almost doubled. It should be noted that the mass spectra shown in Fig. S4 are only for qualitative analysis since the ionisation properties may greatly vary among different chemical species. While the quantitative information was obtained by GC analysis, as demonstrated in the Method section.
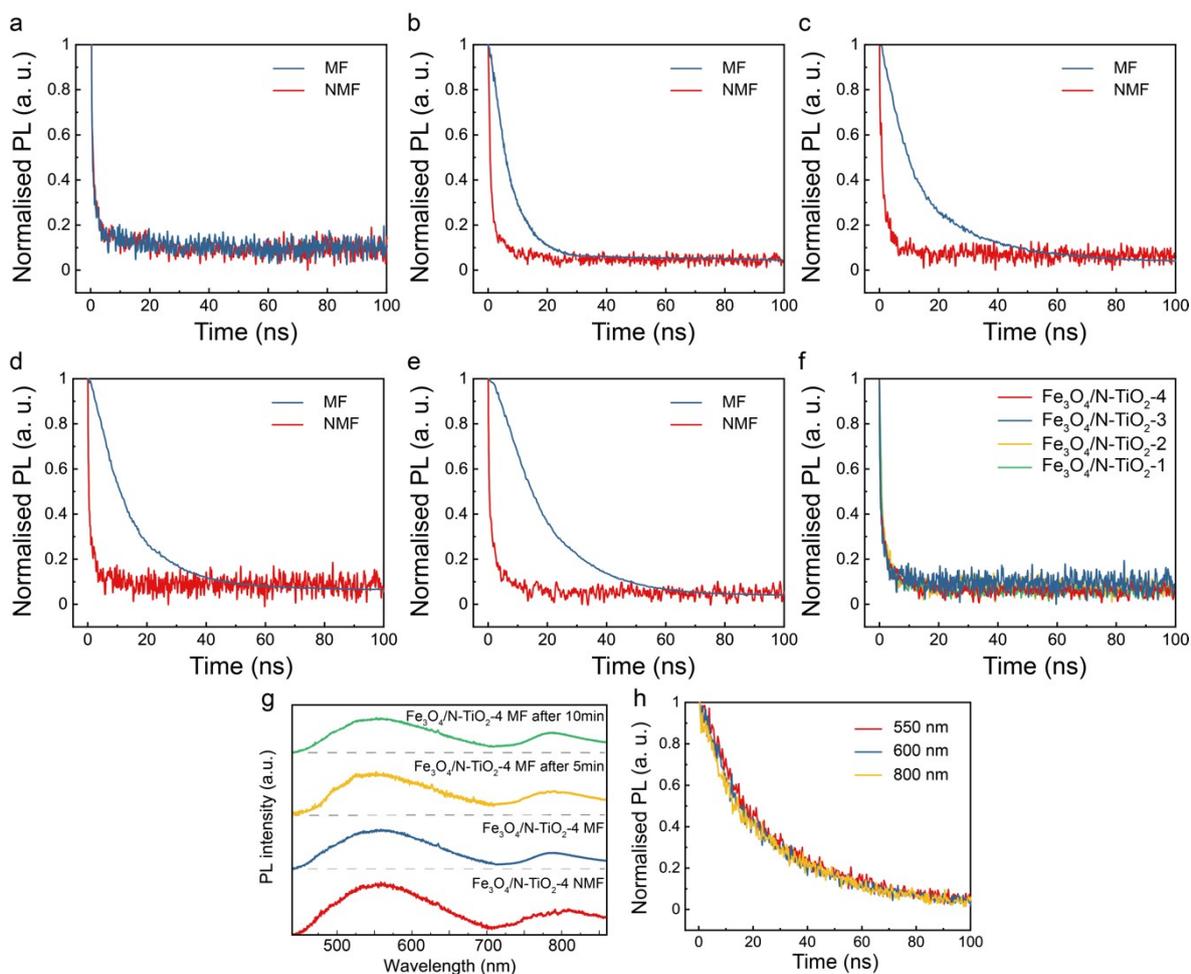
Figure S5 TRPL studies of Fe$_3$O$_4$/N-TiO$_2$ photocatalysts. TRPL spectra of **a** N-TiO$_2$ **b** Fe$_3$O$_4$/N-TiO$_2$-1, **c** Fe$_3$O$_4$/N-TiO$_2$-2, **d** Fe$_3$O$_4$/N-TiO$_2$-3 and **e** Fe$_3$O$_4$/N-TiO$_2$-4 measured with and without an external magnetic field of 180 mT (NMF=no magnetic field; MF=magnetic field). **f** Time-resolved PL spectra of Fe$_3$O$_4$/N-TiO$_2$ photocatalysts without the external magnetic field of 180 mT. The Fe$_3$O$_4$NPs content was set to be 10%, 20%, 30% and 40 wt% as Fe$_3$O$_4$/N-TiO$_2$-1, Fe$_3$O$_4$/N-TiO$_2$-2, Fe$_3$O$_4$/N-TiO$_2$-3 and Fe$_3$O$_4$/N-TiO$_2$-4, respectively. The exciton lifetimes of the photocatalysts are summarised in Supplementary Table 2. **g** PL spectra of Fe$_3$O$_4$/N-TiO$_2$-4 under different conditions. **h** TRPL spectra of Fe$_3$O$_4$/N-TiO$_2$-4 obtained using different probing wavelengths.
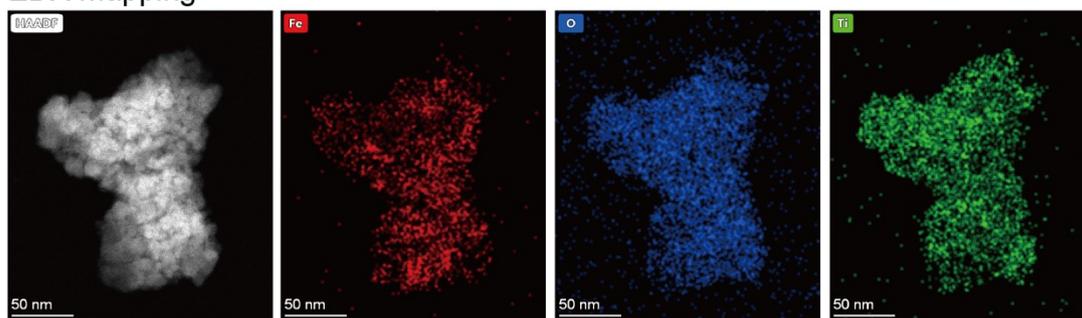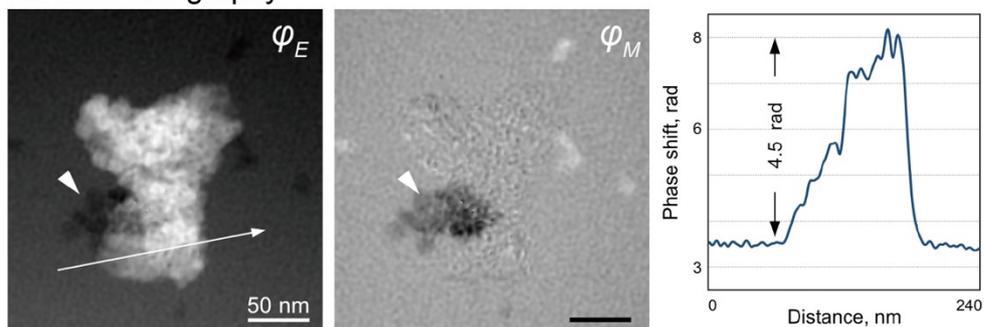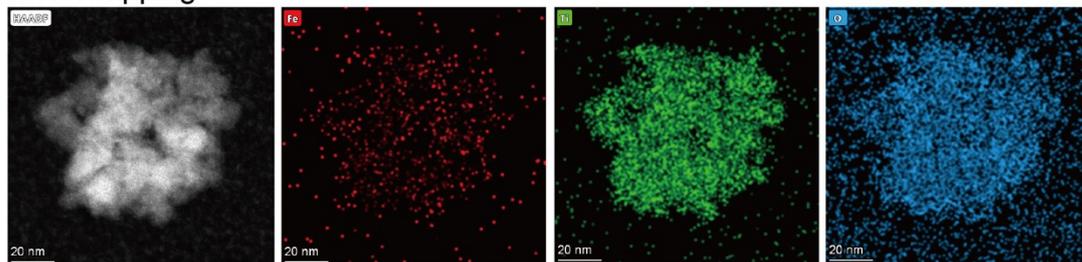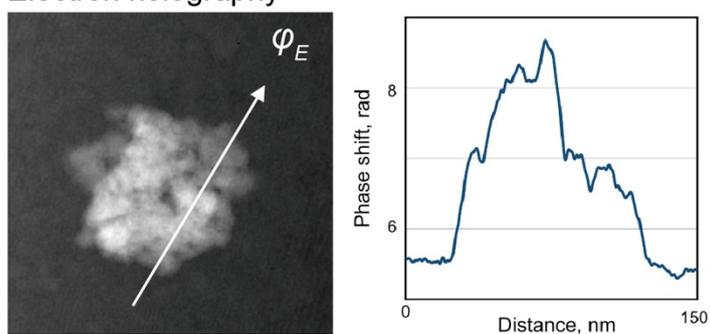
Figure S6 Energy dispersive X-ray spectroscopy (EDS) and the correlative off-axis electron holography studies of the (**a**) Fe_3O_4/N-TiO_2-4 and (**b**) Fe_3O_4/N-TiO_2-2 photocatalysts. The Fe_3O_4NPs content was 20% and 40 wt% for Fe_3O_4/N-TiO_2 and Fe_3O_4/N-TiO_2-4, respectively.
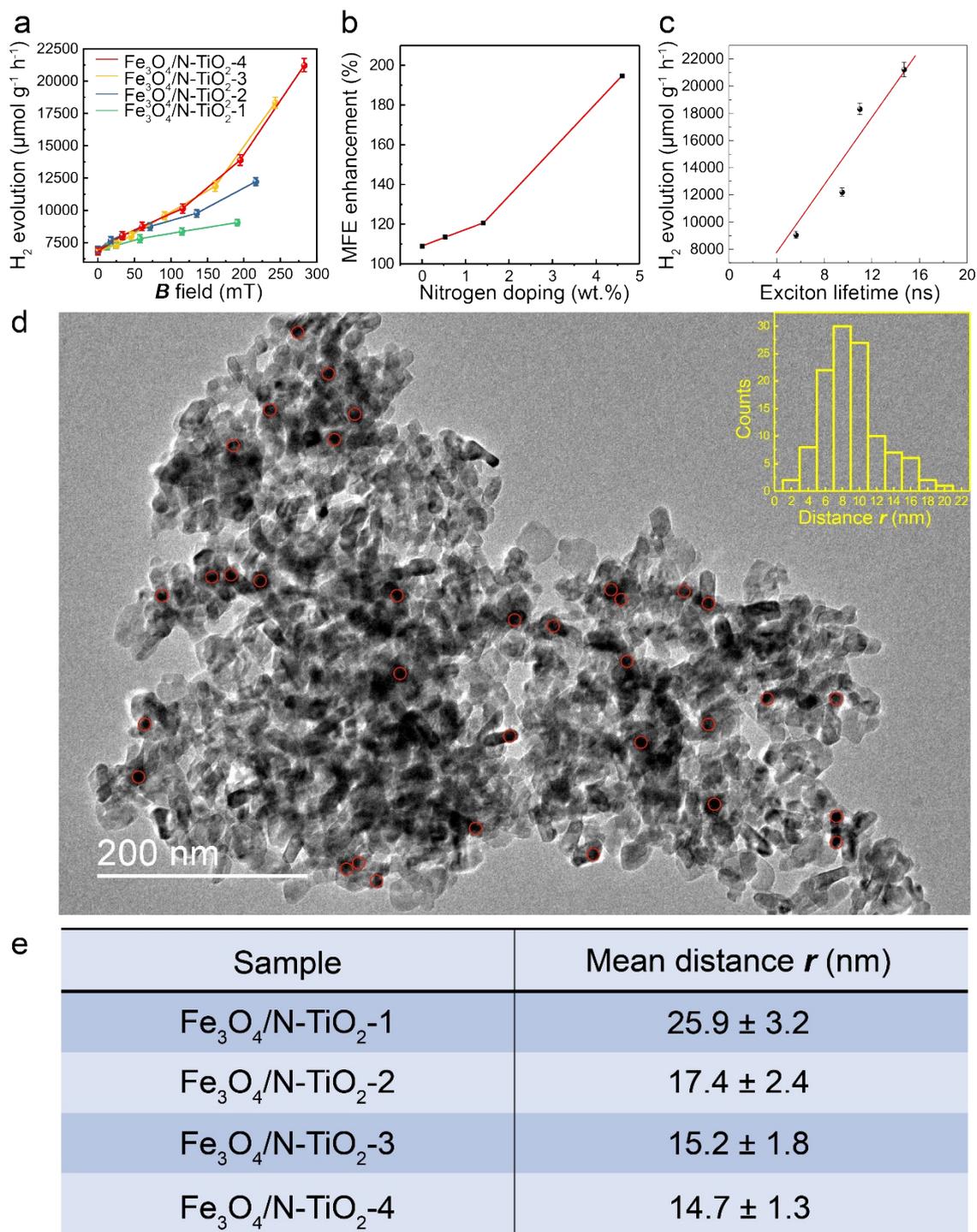
Figure S7 Correlation of the POWS performance and the magnetic field effect. **a** the relationship between the POWS performance of Fe_3O_4/N-TiO$_2$ photocatalysts with different Fe_3O_4 concentration and the local magnetic induction **B**$_{local}$. The magnetic induction **B**$_{local}$ was derived from the M-H curves, using the equation: **B**$_{local}$=μ_0(**M+H**), where μ_0 is the permeability of vacuum space. Apparently, hydrogen evolution rate shows positive correlation with the magnetic induction, which is proportional to the Lorentz force, however, is not in a linear relationship. **b** The POWS performances of the Fe_3O_4/N-TiO$_2$ photocatalysts with different N-doping levels in the N-TiO$_2$, of which the Fe_3O_4 concentrations were all maintained as 40 wt.%, tested with an external magnetic field of 180 mT. The POWS reaction was carried out at 270 °C with the irradiation of a 300-W Xe lamp which included UV and visible light, considering the extremely low absorption of pure TiO$_2$ in the visible light regime. The magnetic field effect (MFE) enhancement of each

catalyst was defined as *[Activity(with magnetic field)-Activity(no magnetic field)]/Activity(no magnetic field),* which clearly shows that the magnetic field introduced moderate effect at low N-doping levels, and became much more significant at high N-doping level, indicating that there are presumably other factors contributing to the magnetic field effect in addition to the Lorentz force, and such factors are greatly influenced by the N-doping concentration. **c** The relationship between the POWS performance and the average exciton lifetime of the Fe_3O_4/N-TiO_2-1, Fe_3O_4/N-TiO_2-2, Fe_3O_4/N-TiO_2-3 and Fe_3O_4/N-TiO_2-4 photocatalysts in an external magnetic field of 180 mT. **d** A typical HRTEM image of Fe_3O_4/N-TiO_2-4, from which the average distance from Fe_3O_4 core to the catalyst surface (**r**) was estimated. More than 100 positions were selected to estimate the average distance **r**, and the distance distribution was shown as inserted. **e** Summary of the average distance *r* (with errors) of each sample. All error-bars indicate the standard deviations. The Fe_3O_4 NPs content was set to be 10 wt.%, 20 wt.%, 30 wt.% and 40 wt.% in the Fe_3O_4/N-TiO_2-1, Fe_3O_4/N-TiO_2-2, Fe_3O_4/N-TiO_2-3 and Fe_3O_4/N-TiO_2-4 photocatalysts, respectively. Details are discussed in Supplementary Discussion 2.
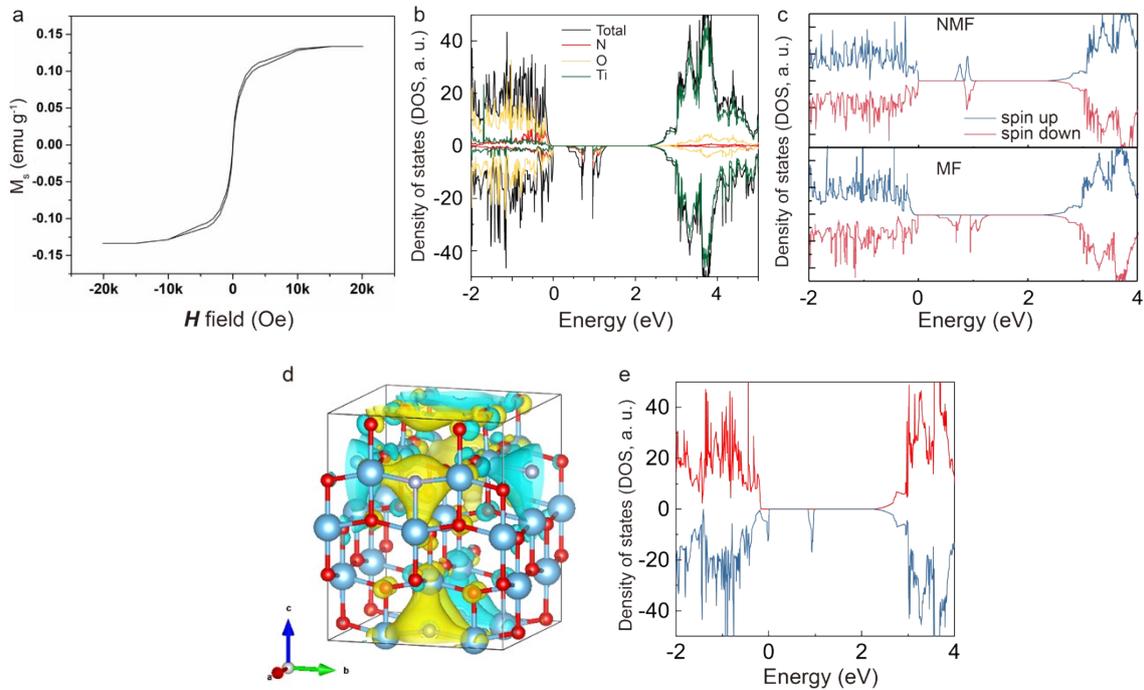
Figure S8 a M-H curve of N-TiO_2 photocatalyst after subtraction of the diamagnetic signal; **b** Calculated partial density of states (PDOS) of the $Ti_{16}O_{28}N_4$ supercell with the external magnetic field alignment; **c** Calculated total DOS of the $Ti_{16}O_{28}N_4$ supercell without and with the external magnetic field (NMF=no magnetic field; MF=magnetic field); **d** 3D spatial distributions of the spin polarisation of N-doped $Ti_{16}O_{28}N_4$ model without any external magnetic field. Yellow surfaces represent the charge density of spin-up electrons and blue surfaces represent the charge density of spin-down electrons. The value of the iso-surface is set to be 0.001eV/Å. **e** Calculated total DOS of the $Ti_{16}O_{31}N$ supercell with lower N-concentration when the external magnetic field is absent.
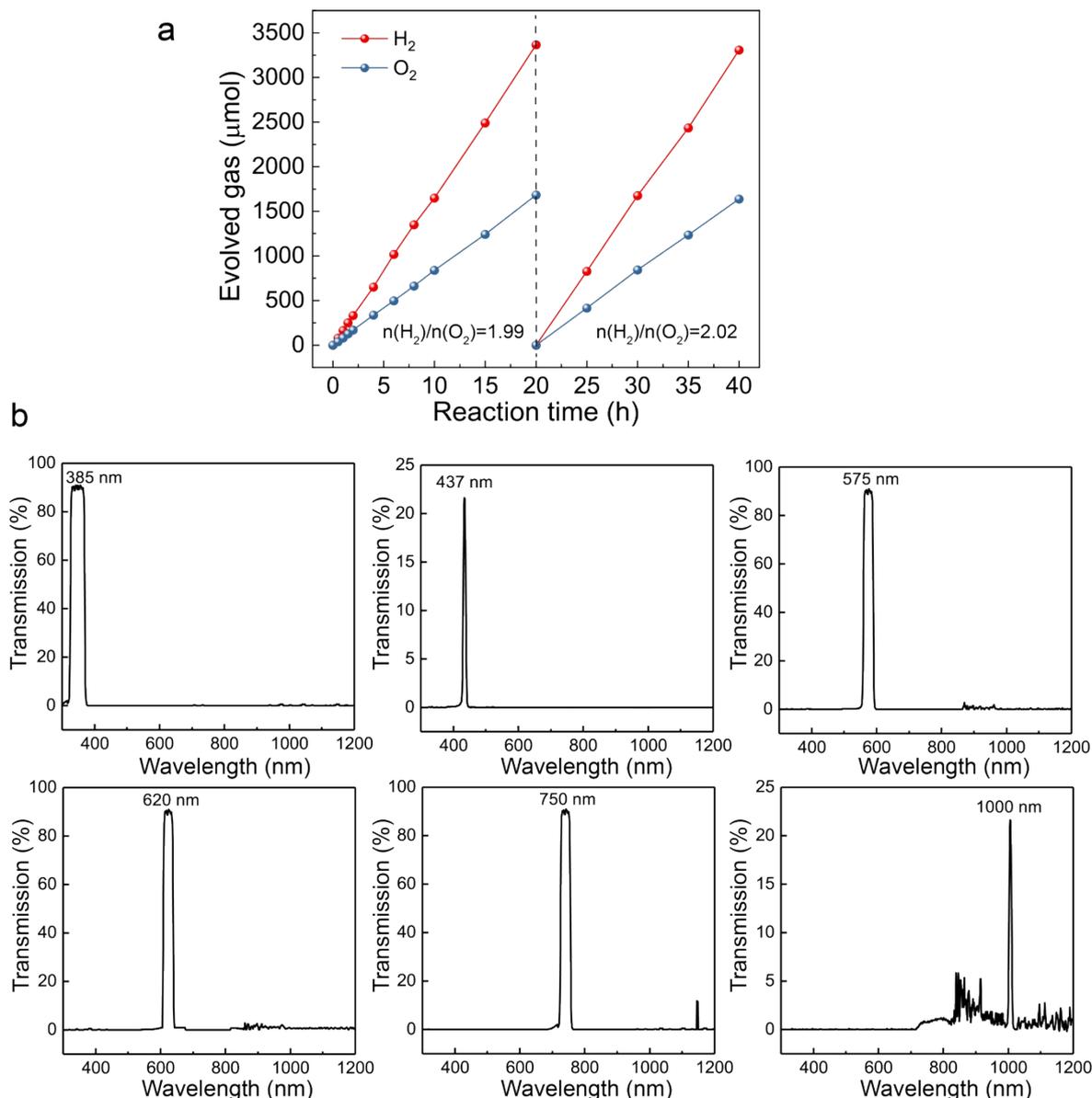
Figure S9 a The stability test of 1 wt.% Au-decorated Fe_3O_4/N-TiO_2-4 photocatalyst for the POWS reaction at 270 °C under simulated solar irradiation and an external magnetic field of 180 mT, indicating a stable and stoichiometric H_2 and O_2 evolution over 20 hours, which is reproducible. For each data point shown in this figure, the reactor was cooled down naturally to room temperature and 1 mL of gaseous phase was sampled for GC analysis. Then the reactor was heated up to 270 °C again for further reaction without any purging in the 20-hour period. **b** UV-vis-NIR transmission spectra of the bandpass filters used for the internal QE evaluations.
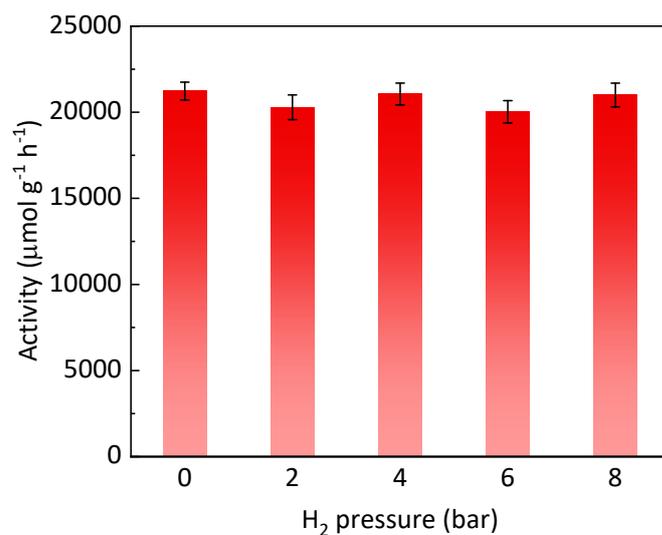
Figure S10 The POWS activity of 1 wt.% Au decorated Fe_3O_4/N-TiO_2-4 at 270 ^oC with a magnetic field of 180 mT in the presence of pre-pressurised pure H_2 with different pressures. All experiments have been performed for 2 hours. The activity of the POWS reaction is represented by the H_2 evolution rate. Clearly, the reaction could still take place even H_2 is pressurised in the reactor, and the activity does not obviously change with the H_2 pressure. Error bars indicate the standard deviations of GC measurements.
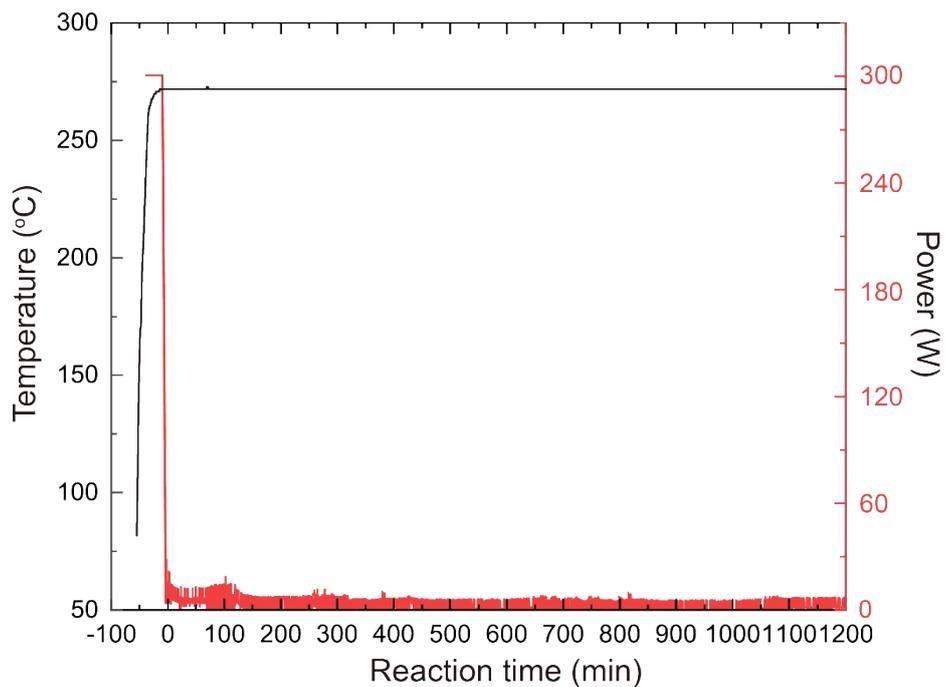
Figure S11 Heating curve of the 20-hour long-term POWS reaction on the Fe_3O_4/N-TiO_2-4 photocatalyst under a magnetic field of 180 mT at 270 °C. The heating process was controlled by a Parr 4838 thermo-controller under the proportional integral derivative (PID) mode and monitored using a SpecView-3 software. The actually energy consumed for heating up the whole system (reactor + reactant + photocatalyst) from 20 to 270 °C and maintaining the temperature at 270 °C for 20 hours can be calculated by integrating the power-time curve, which is shown in detail in Note S2.
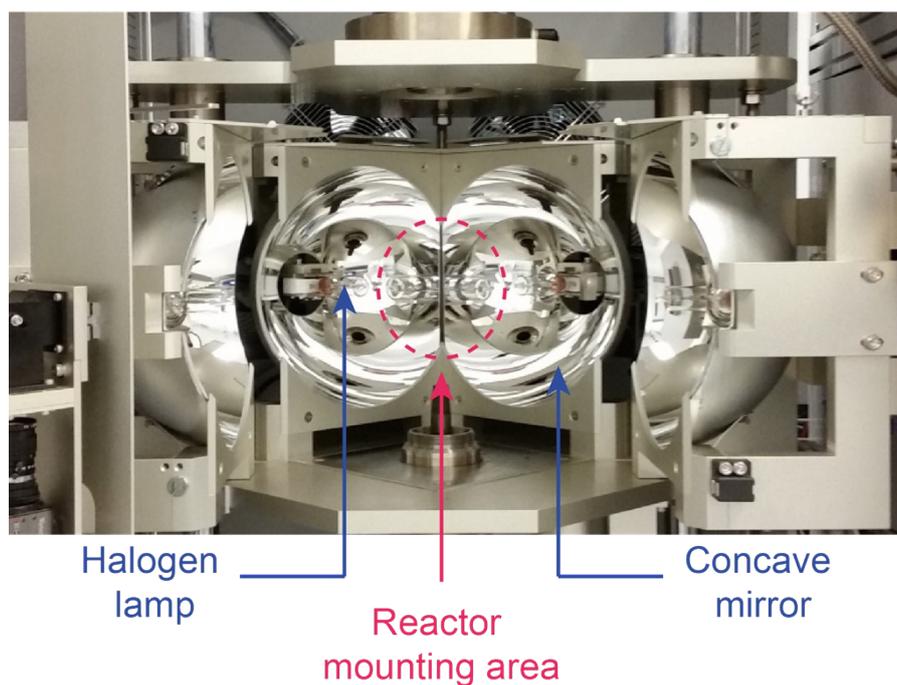
Figure S12 A photographic image of a four-mirror floating-zone light furnace from Crystal Systems Inc. used to demonstrated the idea of solar heating using a solar concentrator to provide both heat and photons to the POWS system at elevated temperatures without any other energy input from an electrical device. The reactor temperature of 270 °C can be maintained by this light source alone, and a H_2 evolution rate of about 7600 μmol g^{-1} h^{-1} is achieved on Fe_3O_4/N-TiO_2-4 for up to 20 h when a magnetic field is absent. The conditions were the same as those for the typical photocatalytic water-splitting activity test, while the light source was generated by the four-mirror floating-zone light furnace (operated at 66.7 V, 15.58 A and 1039 W). After a certain time of reaction, the autoclave was cooled down naturally and the amounts of hydrogen and oxygen were measured by GC.

Table S1 Investigations of the N-doping concentrations based on XPS results.

Photocatalyst	NH$_3$ treatment temperature (^{o}C)	N/Ti molar ratio [a]	N wt.% in N-TiO$_2$ [b]
Fe$_3$O$_4$/N-TiO$_2$-1	625	0.256/1	4.63
Fe$_3$O$_4$/N-TiO$_2$-2	625	0.251/1	4.53
Fe$_3$O$_4$/N-TiO$_2$-3	625	0.249/1	4.51
Fe$_3$O$_4$/N-TiO$_2$-4	625	0.254/1	4.59
40 wt.% Fe$_3$O$_4$/N-TiO$_2$ medium doping	600	0.0806/1	1.41
40 wt.% Fe$_3$O$_4$/N-TiO$_2$ low doping	550	0.0303/1	0.53
40 wt.% Fe$_3$O$_4$/TiO$_2$	/	0	0

[a] the surface N/Ti molar ratios were obtained from the XPS spectra of each material;

[b] Surface N wt.% is calculated based on N-TiO$_2$ using the chemical formula TiO$_{2-1.5x}$N$_x$.

Table S2 Photocatalytic activities of TiO$_2$ based magnetic photocatalysts in this work.

Entry	Photocatalysts	Magnetic field	H$_2$ evolution rate (µmol h^{-1} g^{-1})[b]	H$_2$ to O$_2$ ratio	Turnover number (TON)[c]
1	N-TiO$_2$	/	7024 ± 232	2.07	276 ± 9
2		180 mT	7078 ± 256	1.98	279 ± 10
3	Fe$_3$O$_4$/N-TiO$_2$-1	/	6926 ± 247	2.09	273 ± 10
4		10 mT	7184 ± 258	1.99	283 ± 10
5		20 mT	7282 ± 238	2.03	287 ± 9
6		50 mT	7796 ± 304	1.95	307 ± 12
7		105 mT	8360 ± 287	1.97	329 ± 11
8		180 mT	9058 ± 258	1.99	357 ± 10
9	Fe$_3$O$_4$/N-TiO$_2$-2	/	6954 ± 266	2.10	274 ± 10
10		10 mT	7687 ± 277	2.01	303 ± 11
11		20 mT	8087 ± 281	1.97	319 ± 11
12		50 mT	8744 ± 287	2.06	345 ± 11
13		105 mT	9769 ± 298	2.04	385 ± 12
14		180 mT	12210 ± 307	1.96	481 ± 12
15	Fe$_3$O$_4$/N-TiO$_2$-3	/	6778 ± 255	2.03	267 ± 10
16		10 mT	7370 ± 273	2.03	290 ± 11
17		20 mT	8048 ± 288	2.05	317 ± 11
18		50 mT	9580 ± 305	2.08	377 ± 12
19		105 mT	11870 ± 384	2.01	468 ± 15
20		180 mT	18326 ± 411	1.98	722 ± 16
21	Fe$_3$O$_4$/N-TiO$_2$-4	/	6825 ± 262	2.02	268 ± 10 (2 hrs) TOF=131 h^{-1} (0.5 hr)
22		10 mT	8063 ± 307	2.04	317 ± 12
23		20 mT	8750 ± 332	1.95	345 ± 13
24		50 mT	10130 ± 358	2.08	399 ± 14
25		105 mT	13880 ± 417	2.04	547 ± 16
26		180 mT	21230 ± 520	1.96	836 ± 20 (2 hrs) 13266 ± 43 (20 hrs, 1 Sun) TOF=434 h^{-1} (0.5 hr)

27[a]	Fe$_3$O$_4$/N-TiO$_2$-4	/	9550 $\pm$ 273	2.05	376 $\pm$ 11
28[a]		180 mT	28140 $\pm$ 503	1.95	1109 $\pm$ 20
29[a]	40 wt.% Fe$_3$O$_4$/TiO$_2$	/	1240 $\pm$ 146	2.07	49 $\pm$ 6
30[a]		180 mT	2690 $\pm$ 221	2.03	106 $\pm$ 9
31	Fe$_3$O$_4$@SiO$_2$/N-TiO$_2$-2	/	7108 $\pm$ 211	1.97	280 $\pm$ 8
32	Fe$_3$O$_4$@SiO$_2$	/	/	2.02	/
33		180 mT	/	1.96	/
34	Fe$_3$O$_4$	/	/	2.03	/
35		180 mT	/	1.98	/
36	40 wt.% Fe$_3$O$_4$/N-P25	/	7019 $\pm$ 213	2.01	276 $\pm$ 8
37		180 mT	19620 $\pm$ 356	2.04	771 $\pm$ 14
38	40 wt.% Fe$_3$O$_4$/N-ST-01	/	6958 $\pm$ 192	1.94	274 $\pm$ 8
39		180 mT	19258 $\pm$ 427	2.10	758 $\pm$ 17

[a] the POWS activity tests were carried out using 300-W Xe lamp as the light source which contains UV and visible light;

[b] the hydrogen evolution rates were calculated based on the weight of N-TiO$_2$ and Au contained in the photocatalysts instead of the total weight of Au/Fe$_3$O$_4$/N-TiO$_2$ material. Photocatalysts were used after deposition of 1 wt.% Au via the photo-reduction method. The Fe$_3$O$_4$NPs content was set to be 10 wt.%, 20 wt.%, 30 wt.% and 40 wt.%, as Fe$_3$O$_4$/N-TiO$_2$-1, Fe$_3$O$_4$/N-TiO$_2$-2, Fe$_3$O$_4$/N-TiO$_2$-3 and Fe$_3$O$_4$/N-TiO$_2$-4, respectively.

The amount of hydrogen produced from the POWS reaction under visible light irradiation was measured by GC for 3 times for each entry, and the experimental errors, which indicate the standard deviations of the 3-time repeated GC measurements, are given in this table.

[c] the TON values are calculated for the POWS reaction performed for a certain period of time (typically 2 hours, unless specifically indicated next to the value), based on the molar amount of Au atoms. Besides, when evaluating the TOF values, the reaction was carried out for only 0.5 hour to ensure a low conversion for an accurate evaluation of TOF.

Table S3 Exciton lifetime values and corresponding exponential fitting error of each photocatalyst derived from the time-resolved photoluminescence spectroscopy results in this work. Error in the fitting is determined from its least square.

Entry	Photocatalysts	Magnetic field	τ_1/ns	τ_2/ns	$\tau_{Average}$/ns
1	N-TiO$_2$	/	2.18	/	2.18±0.05
2		180 mT	2.27	/	2.27±0.04
3	Fe$_3$O$_4$/N-TiO$_2$-1	/	2.11	/	2.11±0.03
4		180 mT	2.19	6.45	5.60±0.08
5	Fe$_3$O$_4$/N-TiO$_2$-2	/	2.03	/	2.03±0.02
6		180 mT	2.37	10.71	9.49±0.11
7		105 mT	2.35	9.17	8.03±0.09
8		10 mT	2.87	2.53	2.46±0.05
9	Fe$_3$O$_4$/N-TiO$_2$-3	/	2.24	/	2.24±0.04
10		180 mT	2.73	12.39	10.98±0.11
11	Fe$_3$O$_4$/N-TiO$_2$-4	/	1.98	/	1.98±0.02
12		180 mT	3.04	15.17	14.69±0.13

Table S4 Calculation of the local magnetic flux density for each sample under different applied external magnetic flux density measured by a Gauss meter. *

Photocatalyst	$B_{external}$ (mT)	B_{local} (mT)	B_{local}/r^2 (mT nm^{-2})
N-TiO$_2$	0	0	/
	10	10	/
	20	20	/
	50	50	/
	105	105	/
	180	180	/
Fe$_3$O$_4$/N-TiO$_2$-1	0	0	0
	10	13	0.019
	20	25	0.037
	50	57	0.086
	105	115	0.17
	180	191	0.28
Fe$_3$O$_4$/N-TiO$_2$-2	0	0	0
	10	17	0.058
	20	33	0.11
	50	71	0.24
	105	135	0.45
	180	216	0.71
Fe$_3$O$_4$/N-TiO$_2$-3	0	0	0
	10	25	0.11
	20	46	0.19
	50	91	0.39
	105	160	0.69
	180	243	1.04
Fe$_3$O$_4$/N-TiO$_2$-4	0	0	0
	10	34	0.16
	20	60	0.28
	50	116	0.54
	105	195	0.90
	180	283	1.31

*The external magnetic flux density $B_{external}$ values were measured by Gauss meter and they could be converted into the external field strength, **H** using the equation **H** = $B_{external}/\mu$ − **M**. Subsequently, the

magnetisation (M) value of the Fe_3O_4/N-TiO_2 photocatalysts under such external magnetic field H can be figured out using the corresponding M-H curve (Figs. 1g and 2b). Consequently, the induced local magnetic flux density (B_{local}) can be worked out by considering both the applied external field and the magnetisation of the superparamagnetic Fe_3O_4 NPs, using the equation $B_{local} = \mu(H+M)$. We also considered the distance from the Fe_3O_4 core to the surface of the photocatalyst particle. As shown in Fig. S7d, the distance was evaluated from HR-TEM images and then the local magnetic flux density was corrected with the as-obtained distance (r), giving a B_{local}/r^2 value.

Table S5 Comparison of the POWS performances from selected literatures and the results in this work.

Photocatalyst	H_2 Evolution Rate ($\mu mol\ h^{-1}\ g^{-1}$)	QE (%)	STH (%)	Ref.
Fe_3O_4/N-TiO_2-4	21230 $\pm$ 520	88.7 $\pm$ 2.1 (437 nm)	11.5 $\pm$ 0.3	This work
CoO	/	/	5	3
Co-P/BP	3500	42.55 (430 nm)	5.4	4
$SrTiO_3$:La,Rh and $BiVO_4$:Mo powders	/	33 (419 nm)	1.1	5
Rh/Cr_2O_3/CoOOH /$SrTiO_3$:Al	/	95.9 (360 nm) 33.6 (380 nm)	0.65	6
RhCrO$_x$/$SrTiO_3$:Al	5.6 (mL h^{-1} cm^{-2})	56 (365 nm)	0.4	7

Table S6 Temperature effect on POWS activity over 1 wt.% Au/N-TiO$_2$ photocatalyst at different elevated temperatures. Reproduced from ref. [8]

Temperature (°C)	POWS activity (μmol h^{-1} g^{-1})
220	698 ± 82
230	1524 ± 90
240	3137 ± 92
250	4870 ± 110
260	5768 ± 93
270	6746 ± 163
280	5533 ± 134
290	4253 ± 87

Typically, 5 mg of 1 wt.% Au/N-TiO$_2$ photocatalyst was added to 10 mL of Milli-Q H$_2$O in a 20-mL stainless-steel autoclave equipped with quartz windows under vigorous magnetic stirring, and Ar gas was used as the inert gas. Then the autoclave was heated up to designated temperatures.

Table S7 Thermodynamic calculations for the 20-hour long-term POWS reaction at 270 °C under simulated solar irradiation using 1 wt.% Au decorated Fe$_3$O$_4$/N-TiO$_2$-4 photocatalyst with an external magnetic field of 180 mT.

Reaction time (h)	p_{H_2} (kPa)	p_{O_2} (kPa)	Free energy (kJ mol^{-1})	STH (%)
0.5	17.7	8.6	183.4	10.2
1	37.0	18.9	188.4	10.9
1.5	56.6	28.6	191.2	11.3
2	74.9	38.4	193.1	11.3
4	147.1	75.9	197.7	11.4
6	229.9	112.3	200.7	12.1
8	305.1	149.6	202.6	12.1
10	372.4	189.2	204.0	11.9
15	562.4	280.1	206.8	12.2
20	760.0	380.1	208.8	12.4
Time-average	**/**	**/**	**203.3±5.4**	**11.9±0.5**

Discussion S1. Potential applications of photocatalytic water splitting system at elevated temperatures

When considering the practicality of using elevated temperatures for photocatalysis, we also demonstrated that the high temperature and visible light irradiation can both be provided solely by light with the help of a light-concentrating furnace.[8] Since the light intensity is enhanced greatly in such a configuration, the photocatalytic overall water splitting reaction can also be achieved at 200 °C, giving a promising hydrogen evolution rate as well. Thus, solar concentrators, such as parabolic cylinder reflectors could provide enhanced light irradiation and temperature for small/medium size applications as discussed.[9] Moreover, we have also highlighted that some strategies, for example, the recovery of heat from superheated steam and using a number of possible exothermic coupling reactions with H_2 might provide the heat required for the system at large scale, etc. Exploitation plans have also been devised to address some practical issues for potential applications including the injection of separated H_2 from photocatalytic water splitting at elevated temperature for decentralized domestic devices into natural gas pipeline in UK and some parts of Europe, etc. for caloric use of this renewable fuel. Further preliminary studies showed the feasibility of using water vapour in this photocatalytic process which could be more controllable, easier to operate, possess lower heat capacity (therefore uses less energy to heat up), and can be operated at lower pressure for the same temperature, etc. In another word, substituting liquid water with water vapor in continuous flow systems could make them more practical and feasible at elevated temperatures. It is noteworthy that the visible-light-driven water splitting system clearly works well even with water vapour.[8]

Discussion S2. Potential local thermal effects from the magnetic field

The potential local heating of the superparamagnetic Fe_3O_4 NPs under an external magnetic field is considered in this work. First, from our own past experience, we developed recoverable magnetic core shell nanoparticle catalysts with stronger magnetic susceptibility than that of Fe_3O_4 [10] and other magnetic particles for biological applications [11]. We did not detect any significant rise in temperature in liquid phase under the similar magnetic flux. Similarly, in this paper, the temperature was well controlled at 270 ^oC in superheated water with no notice of any runaway temperature. We believe the application of such small static magnetic field would not cause a significant heating.

On the other hand, according to extensive literature in this area, the thermal effects of magnetic nanoparticles are mainly attributed to Eddy current loss and hysteresis loss.[12,13] The Eddy current loss is caused by the inducing current under the alternative magnetic field according to the Faraday's law of electromagnetic induction.[14] The heat generated by hysteresis loss is caused by the alignment of the magnetic moments with the changing field.[15] However, these two thermal effects mainly occur under alternating magnetic field. In this work, the photocatalytic reactions were carried out under our static magnetic fields provided by parallelly placed permanent magnets, thus, the anticipated small inducing heating may not create an obvious impact on the overall catalytic process.

Moreover, although we cannot fully exclude the possibility that a strong local heating could still take place in the sample. Nevertheless, we have reported a detailed study of the temperature effect of Au-decorated N-doped TiO_2 and found that the optimal temperature for catalysis is at 270 ^oC due to the temperature-dependent water ionic dissociation (Table S6). Any further increase in temperature would cause a decrease in POWS activity. Should the significant thermal effect associated with magnetic field is imposed to our sample, we would anticipate the decrease in the POWS activity rather than a significant enhancement in our results. As a result, we do not feel the induced thermal effects play a key role compared to the magnetic effects that we have attributed.

Discussion S3. Potential kinetic changes due to the magnetic field

It is well known that kinetic rate enhancement could be achieved by thermal effects. However, from our own evaluations, the small and static magnetic field without using alternative magnetic field only exerts marginal associated thermal effect on the photocatalytic rate as compared to the prominently significant direct magnetic effects. Perhaps, the key question is that why the direct magnetic effects can raise the TOF with higher collision frequency on surface reactions for water splitting. As we know, during light illumination, the charge species are constantly created (excitons formation) and destroyed (recombination) in a photocatalyst dynamically such that the lifetime of excitons is a kinetic measure of such dynamic events. It is generally agreed that there are three fundamental possible steps for a typical photocatalytic reaction[16]: 1) photon excitation; 2) charge separation and 3) surface chemical reactions but it is rather difficult to know the nature of rate limiting step in a photocatalytic reaction.

The longest lifetime of excitons may not necessarily lead to an increased TOF if other limiting parameters (i.e. mobility of species) are restricted in the kinetic characteristics in this system. Indeed, there is no strong magnetic effect recorded in our system and other reported systems at room temperature or low operation temperatures. On the other hand, we reported the high working temperature of 270 $^{\circ}$C will remove such kinetic limitations to this POWS system. As mentioned in the manuscript, the water ionic dissociation and kinetic regeneration of the surface oxygen vacancies (V_Os) are greatly promoted at 270 $^{\circ}$C, leading to enhanced concentrations and mobility of fundamental species such as H^+, OH^- and surface V_Os. We have evaluated the kinetics in one of recent reports [17]. In that work, the activation barrier for hydrogen evolution has been calculated to be 60.6 kJ mol^{-1}, which is in good agreement with the activation barrier for oxygen-vacancy formation of 62.5 kJ mol^{-1}, which we derived from variable-temperature EPR. Additionally, this formation energy is in good agreement with the reported activation energy for oxygen-vacancy mobility in anatase of 67.5 kJ mol^{-1},[18] which indicates that the performance of the POWS reaction under such high temperature conditions is no longer limited by the diffusion of bulk oxygen vacancies to surface that is commonly limited at milder temperatures.

When the POWS reaction is operated at elevated temperatures, we have found that the direct magnetic effects are clearly observed. As a result, the larger concentration of fundamental species and higher mobility in bulk phase and on catalyst surface would render the lifetime of charged species important in rate determining for higher TOF (higher dynamic surface concentration). In fact, we have clearly showed that due to the direct local magnetic field effects, the lifetime is greatly prolonged for the Fe_3O_4/N-TiO$_2$ photocatalysts, which is supported by the TRPL measurements (Figs. 2 and S5; Table S3). Besides, the POWS performance is also greatly enhanced accordingly, which shows positive correlation with the lifetime. Therefore, the enhanced photocatalytic activity is attributed to the facilitated charge separation, considering the other important normally rate limiting kinetic parameters have been carefully relaxed and controlled. The TOF is also evaluated by carrying out the POWS reaction using Fe_3O_4/N-TiO$_2$-4 for 0.5 hour to ensure a low conversion, with and without an external magnetic field of 180 mT. The TOF values are evaluated and summarised in Table S2. As shown in the Entry 5 of Table S2, the TOF is greatly enhanced from 131 h^{-1} to 434 h^{-1} for Fe_3O_4/N-TiO$_2$-4 upon the application of an external magnetic field of 180 mT. Along with the TRPL results, it is clearly that due to the greatly prolonged lifetime of the photo-generated electron-hole pairs, more photoelectrons could migrate from the bulk to the surface and accumulate on the Au NPs, which enables more catalytic cycles at a specific catalytic centre without the limitation by the hole regeneration in a given time. It should be emphasised all the POWS reaction is carried out at 270 $^{\circ}$C

in this work, and as demonstrated before, the thermal effects induced by the associated magnetic effect is not significant under the conditions.

Note S1 Calculation of QE

A typical QE calculation is shown below, taking Fe_3O_4/N-TiO_2-4 as an example:

The hydrogen amount analysed by GC is 5.25 µmol, corresponding to 3.159×10^{18} hydrogen molecules;

During a period of 2 hours, the energy of the light irradiation: W=P×t

With the bandpass filter of 437 nm, the light irradiation power is measured to be P=0.45 mW, therefore, the energy W=0.00045×7200=3.24 J, which contains the photon (437 nm) numbers of 7.123×10^{18}.

QE (%) = (2×3.159×10^{18})/ (7.123×10^{18}) ×100% = 88.7 %

Each QE measurement was repeated for at least 3 times and the average value and standard deviation were therefore calculated.

We have also evaluated the internal QE in a NIR regime, as shown in Fig. 4. Using the calculated thermodynamic parameters summarised in Table S7 where the partial pressure changes have been considered, the reaction potential could also be calculated. For a QE measurement, the reaction has been performed for 2 hours and the products were measured by GC likewise. Thus, the time-averaged free energy can be calculated and the resulted reaction potential is 0.979 V. As in the energy evaluation of solar conversion systems by Ross and Bolton, there is always an energy difference of 0.2-0.3 eV between the absorbed photon energy and the energy that can do useful work.[19,20] Thus, the threshold wavelength λ_t which is just capable of driving the reaction can be calculated based on the equation (assuming an energy loss of 0.3 eV):[20,21]

$$\lambda_t = \frac{hc}{\dfrac{\Delta G^\theta}{n} + U_{loss}}$$

The result is ca. 970 nm, which means only the photons with a wavelength shorter than 970 nm can drive the POWS reaction. Bolton et al. gave an example in their work:[20] for a reaction with a potential of 1.052 V, the threshold wavelength λ_t is 880 nm. In our case, the reaction potential is 0.979 V for a 2-hour reaction, which is smaller than that in the example. Thus, the calculated threshold wavelength of 930 nm is reasonable.

Note S2 Calculation of energy efficiencies

a. **Calculation of the Gibbs free energy at 298 K and 101.325 kPa**

   For the reaction:

$$H_2O \text{ (l)} == H_2 \text{ (g)} + 0.5O_2 \text{ (g)}$$
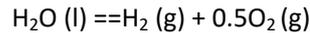
The standard enthalpy of reaction is:

$$\Delta_r H_m^{\ominus} = 0 + 0.5 \times 0 - (-286) = 286 \ kJ/mol$$

The standard entropy change of reaction is:

$$\Delta_r S_m^{\ominus} = 130.684 + 0.5 \times 205.138 - 69.91 = 163.343 \ J/(mol \cdot K)$$

According to the equation of Gibbs free energy:

$$\Delta_r G_m^{\ominus} = \Delta_r H_m^{\ominus} - T\Delta_r S_m^{\ominus}$$

The standard Gibbs free energy at 298 K is:

$$\Delta_r G_m^{\ominus} = 286 - 298 \times 163.343 \times 10^{-3} = 237 \ kJ/mol$$

b. **Calculation of the Gibbs free energy at 543 K and 101.325 kPa**

According to the Van't Hoff equation:

$$\frac{d \ln K}{d T} = -\frac{\Delta H^{\ominus}}{RT^2}$$

Therefore,

$$\ln \frac{K_2}{K_1} = -\frac{\Delta H^{\ominus}}{R}(\frac{1}{T_2} - \frac{1}{T_1})$$

Also, because

$$\Delta_r G_m^{\ominus} = -RT\ln K$$

Then

$$-\frac{\Delta_r G_m^{\ominus}(T_2)}{T_2} + -\frac{\Delta_r G_m^{\ominus}(T_1)}{T_1} = -\frac{\Delta H^{\ominus}}{R}(\frac{1}{T_2} - \frac{1}{T_1})$$

Thus, the Gibbs free energy at 543 K and 101.325 kPa can be calculated:

$$\Delta_r G_m^{\ominus}(543K) = 196.73 \ kJ/mol$$

The reactant at 270 °C in our system is still liquid water, which is under the saturated vapour pressure of ca. 60 bar at 270 °C. Thus, the phase change from liquid water to water vapour is not considered, since this process is not involved in the reaction. As the result shows, the Gibbs free energy at 270 °C (543 K) indeed

decreases by about 40 kJ/mol, but it is still much higher than zero, which means the reaction is still not thermodynamically favourable at this temperature.

c. Correction of the Gibbs free energy for the reaction pressure

According to the Van't Hoff isotherm:

$$\Delta_r G_m = \Delta_r G_m^\ominus + RT \ln Q$$

where $\Delta_r G_m$ is the Gibbs free energy of reaction under non-standard states at temperature T; $\Delta_r G_m^\ominus$ is the Gibbs free energy of the reaction at T and 101.325 kPa; Q is the thermodynamic reaction quotient.

For the POWS reaction, Q can be defined as:

$$Q = \frac{p_{H_2}}{p^\ominus} \cdot \left(\frac{p_{O_2}}{p^\ominus}\right)^{0.5}$$

Also, assuming the gas phase in the batch reactor follows the ideal gas law:

$$p_{H_2} V = n_{H_2} RT$$

Based on the reaction stoichiometry,

$$p_{H_2} = 2p_{O_2}$$

It should be emphasised that our POWS system was conducted at constant temperature (T=543 K) and volume (V=20 mL), thus, the Helmholtz free energy, ΔA, was then used in the subsequent calculation of the efficiencies. Given that:

$$A = U - TS$$

$$G = A + PV$$

It is also noticed that in our system, the partial pressures of H_2 and O_2 change over the reaction progress, resulting in a changing free energy. Therefore, the free energy has been corrected for different partial pressures throughout the whole reaction process of 20 hours, and the STH efficiencies were calculated accordingly, as shown in Fig. 4 and Table S7. Consequently, the average free energy and average STH over the reaction progress are calculated:

$$Time - average\ \Delta A = 203.3 \pm 5.4\ kJ\ mol^{-1}$$

$$Time - average\ \eta_{STH} = 11.9 \pm 0.5\ \%$$

d. Evaluation of the energy input required for heating

Additionally, we have estimated the energy required to heat your system to 270 °C. Considering a photocatalytic process operated under steady state at 270 °C, energy is required to heat the input liquid water from room temperature 25 °C to 270 °C. The energy for heating the reactor is not considered in this calculation since this is not an intrinsic property of the POWS reaction and highly dependent on the reactor design; also, when the system is operating under a steady state, energy is only required to compensate the heat loss, which can be minimised by covering the reactor with adiabatic materials, then this part of energy could presumably be negligible. In our system, 5 mL of water was used as the reactant when the energy efficiencies were evaluated.

When water is heated to 270 °C, the saturated vapour pressure is established, which can be calculated according to the Clausius–Clapeyron relation:

$$\frac{dP}{dT} = \frac{PL}{T^2 R}$$

where P is the pressure, R is the specific gas constant, L is the specific latent heat of the substance, and T is the temperature.

Assuming L is independent to the temperature, then the relation can be integrated, giving:

$$\ln \frac{P_2}{P_1} = -\frac{L}{R}(\frac{1}{T_2} - \frac{1}{T_1})$$

For water, L=40.68 kJ/mol, thus, the saturated vapour pressure at 270 °C is:

$$P(543\ K) = 60.36\ bar$$

Assuming it follows the ideal gas law, the amount of H_2O in the gas phase is:

$$n_{vapour} = \frac{pV}{RT} = \frac{60.36 \times 101.325\ kPa \times 0.015\ L}{8.314 \times 543\ K} = 0.02\ mol$$

$$m_{vapour} = 0.02\ mol \times 18\frac{g}{mol} = 0.36\ g$$

Clearly, only a small portion of water transfers to vapour. Thus, the energy for heating the 5 mL of H_2O from room temperature to 270 °C is calculated as follows, assuming the heat capacity does not significantly change with temperature:

From 25 °C to 100 °C:

$$Q_1 = m_{water}C_{p,\ water}\Delta T = 5\ g \times 4.184\frac{J}{g \cdot K} \times 75\ K = 1569\ J$$

At 100 °C:

$$Q_2 = nL = 0.02\ mol \times 40680\frac{J}{mol} = 813.6$$

From 100 °C to 270 °C:

$$Q_3$$

$$= m_{water}C_{p,\ water}\Delta T + m_{vapour}C_{p,\ vapour}\Delta T = 4.64\ g \times 4.184\frac{J}{g \cdot K} \times 170\ K + ($$
$$= 3413.56\ J$$

Therefore, the total energy required for heating is:

$$Q_{water} = Q_1 + Q_2 + Q_3 = 5796\ J$$

The above has shown the energy required to heat water up to 270 °C. Moreover, we also evaluated the actual overall energy conversion efficiency, $\eta_{overall}$, experimentally. We tried our best to cover the experimental set-up with band heater and thermally insulating materials such as silica wool, thermal foil, etc., to reduce the heat loss, however, a 'perfect' insulation layer cannot be achieved and the heat loss is inevitable. The heating process was controlled by a Parr 4838 thermo-controller under the proportional integral derivative (PID) mode and monitored with a SpecView-3 software (Fig. S11). When the temperature reached 270 °C, the heater started to operate at a low output level to compensate the heat

loss. Thus, the actual energy input could be calculated by integrating the power-time curve and the actual overall energy conversion efficiency can be obtained.

The actually energy consumed for heating up the whole system (reactor + reactant + photocatalyst) from 20 to 270 °C and maintaining the temperature at 270 °C for 20 hours is:

$$Q_{actual} = 53174\,J$$

The energy input from the solar simulator is:

$$E_{solar} = P \cdot \pi \cdot r^2 \cdot t = 5652\,J$$

Subsequently, the actual overall energy conversion efficiency can be calculated:

$$\eta_{overall} = \frac{n_{hydrogen} \times average\ free\ energy\ (543K)}{E_{solar} + Q_{actual}} \times 100\% = 1.16 \pm 0.05\%$$

Although the $\eta_{overall}$ of 1.16 % appears to be quite low, it should be emphasised this is not the situation we anticipate. The heat consumption for heating the system could be excluded in an ideal future setup, in which scenario the heat is not provided by external source but from concentrated solar light in future installation as stated in the manuscript. Such idea of concentrated solar heating has been demonstrated in this work using a light concentrating furnace (Fig. S12). Further fabrication of a larger solar heating POWS system is also in progress. It is apparent that solar light could provide heat by photothermal effect which has been extensively studied. Also, we have previously demonstrated that such energy required for heating the system could come from the waste heat from other processes, such as the exothermic chemical reactions like ammonia synthesis or CO_2 hydrogenation reactions when these processes are coupled together.[8] In addition, the superheated water carries quite large thermal energy, which may subsequently be used for additional energy generation i.e. H_2 by steam turbine-electrolyser. Thus, by considering the availability of solar heating and additional H_2 input, the ultimate $\eta_{overall}$ could be much higher upon further optimisation.

Besides, by comparing the Q_{water} and Q_{actual}, it is obvious that the majority of the energy input is consumed by heating the reactor instead of the reactant, and this part of energy could vary greatly between different reactor designs. Also, the system could be working for even longer period of time without the need of heating up the reactor again, but only a small amount of energy is required to compensate the heat loss (given that a perfect thermal insulation is hardly achievable). In addition, the current $\eta_{overall}$ over a 20-hour reaction is already superior to the recently reported values in literature in the related fields[6,22].

References

1   P. Diehle, A. Kovács, T. Duden, R. Speen, K. Žagar Soderžnik and R. E. Dunin-Borkowski, *Ultramicroscopy*, 2021, **220**, 113098.

2   Y. K. Peng, C. N. P. Lui, Y. W. Chen, S. W. Chou, E. Raine, P. T. Chou, K. K. L. Yung and S. C. E. Tsang, *Chem. Mater.*, 2017, **29**, 4411–4417.

3   L. Liao, Q. Zhang, Z. Su, Z. Zhao, Y. Wang, Y. Li, X. Lu, D. Wei, G. Feng, Q. Yu, X. Cai, J. Zhao, Z. Ren, H. Fang, F. Robles-Hernandez, S. Baldelli and J. Bao, *Nat. Nanotechnol.*, 2014, **9**, 69–73.

4   B. Tian, B. Tian, B. Smith, M. C. Scott, R. Hua, Q. Lei and Y. Tian, *Nat. Commun.*, 2018, **9**, 1397.

5   Q. Wang, T. Hisatomi, Q. Jia, H. Tokudome, M. Zhong, C. Wang, Z. Pan, T. Takata, M. Nakabayashi, N. Shibata, Y. Li, I. D. Sharp, A. Kudo, T. Yamada and K. Domen, *Nat. Mater.*, 2016, **15**, 611–615.

6   T. Takata, J. Jiang, Y. Sakata, M. Nakabayashi, N. Shibata, V. Nandal, K. Seki, T. Hisatomi and K. Domen, *Nature*, 2020, **581**, 411–414.

7   Y. Goto, T. Hisatomi, Q. Wang, T. Higashi, K. Ishikiriyama, T. Maeda, Y. Sakata, S. Okunaka, H. Tokudome, M. Katayama, S. Akiyama, H. Nishiyama, Y. Inoue, T. Takewaki, T. Setoyama, T. Minegishi, T. Takata, T. Yamada and K. Domen, *Joule*, 2018, **2**, 509–520.

8   Y. Li, Y.-K. Peng, L. Hu, J. Zheng, D. Prabhakaran, S. Wu, T. J. Puchtler, M. Li, K.-Y. Wong, R. A. Taylor and S. C. E. Tsang, *Nat. Commun.*, 2019, **10**, 4421.

9   B. A. Pinaud, J. D. Benck, L. C. Seitz, A. J. Forman, Z. Chen, T. G. Deutsch, B. D. James, K. N. Baum, G. N. Baum, S. Ardo, H. Wang, E. Miller and T. F. Jaramillo, *Energy Environ. Sci.*, 2013, **6**, 1983–2002.

10   S. C. Tsang, V. Caps, I. Paraskevas, D. Chadwick and D. Thompsett, *Angew. Chem. Int. Ed.*, 2004, **43**, 5645–5649.

11   S. C. Tsang, C. H. Yu, X. Gao, K. Tam, *,† Shik Chi Tsang, † Chih Hao Yu, †,‡ and Xin Gao and K. Tam§, *J. Phys. Chem. B*, 2006, **110**, 16914–16922.

12   A. Ito, M. Shinkai, H. Honda and T. Kobayashi, *J. Biosci. Bioeng.*, 2005, **100**, 1–11.

13   R. A. Frimpong and J. Z. Hilt, *https://doi.org/10.2217/nnm.10.114*, 2010, **5**, 1401–1414.

14   A. Attaluri, S. K. Kandala, H. Zhou, M. Wabler, T. L. DeWeese and R. Ivkov, *https://doi.org/10.1080/02656736.2020.1798514*, 2021, **37**, 108–119.

15   A. Chiu-Lam and C. Rinaldi, *Adv. Funct. Mater.*, 2016, **26**, 3933–3941.

16   Q. Wang and K. Domen, *Chem. Rev.*, 2020, **120**, 919–985.

17   C. Foo, Y. Li, K. Lebedev, T. T. Chen, S. Day, C. Tang and S. C. E. Tsang, *Nat. Commun.*, 2021, **12**, 661.

18   A. G. Thomas, W. R. Flavell, A. K. Mallick, A. R. Kumarasinghe, D. Tsoutsou, N. Khan, C. Chatwin, S. Rayner, G. C. Smith, R. L. Stockbauer, S. Warren, T. K. Johal, S. Patel, D. Holland, A. Taleb and F. Wiame, *Phys. Rev. B*, 2007, **75**, 035105.

19   R. T. Ross and T. L. Hsiao, *J. Appl. Phys.*, 1977, **48**, 4783–4785.

20   J. R. Bolton, S. J. Stricklert and J. Connolly, *Nature*, 1985, **316**, 495–500.

21   J. R. Bolton, *Science*, 1978, **202**, 705–711.

22   H. Nishiyama, T. Yamada, M. Nakabayashi, Y. Maehara, M. Yamaguchi, Y. Kuromiya, H. Tokudome, S. Akiyama, T. Watanabe, R. Narushima, S. Okunaka, N. Shibata, T. Takata, T. Hisatomi and K. Domen, *Nature*, , DOI:10.1038/s41586-021-03907-3.